High resolution mapping of methane emissions from marine and terrestrial sources using a Cluster-Tuned Matched Filter technique and imaging spectrometry

Andrew K. Thorpe [a,*], Dar A. Roberts [a], Eliza S. Bradley [a], Christopher C. Funk [b], Philip E. Dennison [c], Ira Leifer [d]

[a] Department of Geography, University of California, Santa Barbara, CA, United States
[b] U.S. Geological Survey and Climate Hazards Group, Department of Geography, University of California, Santa Barbara, CA, United States
[c] Department of Geography and Center for Natural and Technological Hazards, University of Utah, Salt Lake City, UT, United States
[d] Marine Science Institute, University of California, Santa Barbara, CA, United States

ARTICLE INFO

ABSTRACT

In this study, a Cluster-Tuned Matched Filter (CTMF) technique was applied to data acquired by the Airborne Visible/Infrared Imaging Spectrometer (AVIRIS) over marine and terrestrial locations known to emit methane (CH_4). At the Coal Oil Point marine seep field, prominent CH_4 anomalies were consistent with advection from known areas of active seepage. For a region with natural CH_4 and oil seepage located west of downtown Los Angeles, significant CH_4 anomalies were identified for known sources at the La Brea Tar Pits and in close proximity to probable sources, including an office complex documented as venting CH_4 continuously and hydrocarbon storage tanks on the Inglewood Oil Field. However, interpretation of anomalies was complicated by noise and false positives for surfaces with strong absorptions at the same wavelengths as CH_4 absorption features. Segmentation of results identified 16 distinct locations of contiguous pixels with high CTMF scores and segments were classified into probable CH_4 anomalies and confusers based on the spectral properties of the underlying surface over the full spectral range measured by AVIRIS. This technique is particularly well suited for application over large areas to detect CH_4 emissions from concentrated point sources and should permit detection of additional trace gasses with distinct absorption features, including carbon dioxide (CO_2) and nitrous oxide (N_2O). Thus, imaging spectrometry by an AVIRIS-like sensor has the potential to improve high resolution greenhouse gas mapping, better constraining local sources.

© 2013 Elsevier Inc. All rights reserved.

1. Introduction

Methane (CH_4) is a long-lived greenhouse gas with an average atmospheric residence of approximately 7.9 years (Lelieveld et al., 1998). One molecule of CH_4 is 72 times more effective at trapping radiant energy than a molecule of carbon dioxide (CO_2) on a 20 year time scale (IPCC, 2007). Global atmospheric CH_4 has more than doubled in the last two centuries with an annual growth rate that has been highly variable since the 1990s with renewed growth starting in 2007 (Dlugokencky et al., 2009) and average concentrations exceeding 1.8 ppm in 2012 (NOAA, 2012).

Emission sources and sinks exhibit high spatial heterogeneity and large-scale interannual variability (Bousquet et al., 2006) and estimates for total sources of atmospheric CH_4 have considerable uncertainty, ranging between 500 and 600 Tg year^{-1} (IPCC, 2007). Between 60 and 70% of CH_4 emissions are presently anthropogenic (Lelieveld et al., 1998) and include emissions from domestic ruminants, rice agriculture, waste handling, and fossil fuel production. Wetlands, termites, and geological seeps are significant natural sources (Etiope et al., 2009), while major CH_4 sinks include oxidization by the hydroxyl radical (OH), loss to the stratosphere, and consumption by methanotrophs in soils (Lelieveld et al., 1998). Approximately 90% of CH_4 destruction is due to OH oxidation (Lelieveld et al., 1993), however, CH_4 destruction is minimal on the time scale of minutes to hours relevant to studying local emissions nearby the source.

On global scales, partitioning between natural and anthropogenic CH_4 sources remains uncertain and emission estimates for individual source categories can vary by as much as a factor of two (Dlugokencky et al.,

2011). On regional scales, uncertainties for anthropogenic CH_4 emissions are considerable, between 9 and 17% in the United States (EPA, 2011) and 19 and 36% for a number of countries in northwest Europe (Bergamaschi et al., 2010).

CH_4 has strong rotational-vibrational transitions causing absorption in the mid-infrared (MIR) and thermal-infrared (TIR), permitting detection by satellite sensors like the Infrared Atmospheric Sounding Interferometer (IASI: Aires et al., 2002), the Tropospheric Emission Spectrometer (TES: Beer et al., 2001), and the Atmospheric Infrared Sounder (AIRS: Tobin et al., 2006). Because detection in the TIR requires a strong thermal contrast between ground and lower atmosphere and is limited by sensor saturation due to a high CH_4 absorption coefficient, current sensors cannot provide near-surface concentrations.

In addition to absorptions in the TIR, CH_4 has absorptions in the shortwave infrared (SWIR) between 1400 and 2500 nm (Fig. 1, top). In this region, water vapor has considerable spectral overlap with CH_4, particularly beyond 2300 nm, which complicates CH_4 detection (Fig. 1, bottom). These SWIR absorptions enabled global CH_4 mapping by the Scanning Imaging Absorption Spectrometer for Atmospheric Chartography (SCIAMACHY) onboard the Envisat satellite, a grating spectrometer with eight channels operating from 240 to 2,400 nm with a spectral resolution between 0.2 to 1.4 nm and spatial resolution ranging from 30×60 km to 30×240 km (Buchwitz et al., 2004). The Weighting Function Modified Differential Optical Absorption Spectroscopy (WFM-DOAS) retrieval algorithm (Buchwitz et al., 2000) was applied to 2003 data from SCIAMACHY channels 4, 6, and 8 to estimate column amounts of CO (carbon monoxide), CO_2, and CH_4 (Buchwitz et al., 2005). Frankenberg et al. (2005) developed an iterative maximum a posteriori-DOAS (IMAP-DOAS) algorithm using DOAS and the linear relationship between vertical column-densities for CO_2 and CH_4 to estimate global CH_4 column-averaged mixing ratios over terrestrial surfaces and detect regions with high column averages, including the Red Basin in China and the Sudd wetlands of southern Sudan

(Frankenberg et al., 2011). While the Envisat satellite mission ended in 2012, the Greenhouse Gas Observing Satellite (GOSAT: Saitoh et al., 2009) continues to provide global CH_4 mapping in good agreement with ground based measurements (Butz et al., 2011) and results from global 3-D chemical transport models (Parker et al., 2011).

Global CH_4 concentrations are well constrained due to existing spaceborne remote sensing that provides an effective means of detecting continental scale variation in CH_4 concentrations. However, spaceborne sensors lack the fine spatial resolution needed to detect near-surface emissions. Local emission monitoring typically relies upon ground-based measurements with limited spatial coverage, such as gas chromatography, tunable diode lasers (Hsu et al., 2010), or Fourier transform spectrometers at fixed sites (Wunch et al., 2009). Airborne sensors could provide valuable data for constraining emissions at local to regional scales (NRC, 2010). Improved constraint of emissions at these scales is critical for improving national greenhouse gas budgets and the partitioning between anthropogenic and natural sources (Bovensmann et al., 2010). Airborne measurements could also help address discrepancies between top-down and bottom-up estimates of emissions (Montzka et al., 2011) and complement ongoing global monitoring efforts at coarser spatial resolutions (Schepers et al., 2012).

Airborne imaging spectrometers are well suited for monitoring local sources because they can provide coverage over large regions with the fine spatial resolution necessary to resolve point source emissions. The Airborne Visible Infrared Imaging Spectrometer (AVIRIS) measures reflected solar radiance across 224 contiguous spectral bands between 350 and 2500 nm with a signal-to-noise ratio that should permit CH_4 mapping (Leifer et al., 2006b). Roberts et al. (2010) used AVIRIS data acquired over the Coal Oil Point (COP) seep field in the Santa Barbara Channel, California to calculate spectral residuals for CH_4 above background and a CH_4 index derived from the average residual between 2248 and 2298 nm. Although strong CH_4 anomalies were detected in close proximity to known seeps, mapping proved challenging given results were overly sensitive to albedo (Roberts et al., 2010).

Using a high-glint AVIRIS scene acquired over COP, Bradley et al. (2011) developed a band ratio technique using radiance for a CH_4 absorption band (2298 nm) and a CO_2 absorption band (2058 nm) to generate the AVIRIS CH_4 index, ζ (L_{2298}/L_{2058}). In the absence of strong local sources of CH_4 or CO_2, these gasses are well mixed and a regression of CH_4 and CO_2 bands produces a straight line. If additional CH_4 above background is present in the lower boundary layer and CO_2 is well mixed, radiance for the CH_4 band decreases due to increased absorption, resulting in a lower CH_4 to CO_2 band ratio. Despite variations in surface albedo, this method clearly detected a CH_4 plume that was consistent with wind advection from a sonar-quantified source (Bradley et al., 2011).

While Roberts et al. (2010) and Bradley et al. (2011) demonstrate that CH_4 from marine sources can be detected using AVIRIS scenes with high sunglint, these techniques cannot be applied to terrestrial locations that rarely exceed 50% albedo, where the majority of anthropogenic emissions occur (NRC, 2010). Although water can often be assumed spectrally flat in the SWIR (Roberts et al., 2010), this assumption is unrealistic for most land cover types. Spectral variation in surface reflectance arising from heterogeneous land cover invalidates the use of a ratio, where a change in radiance at 2298 nm relative to 2058 nm could either be a product of changing CH_4 or CO_2 absorption, or a change in surface reflectance with wavelength.

This study aims to improve methods for detecting absorption features of CH_4, thereby permitting high spatial resolution mapping of local emissions over marine environments and heterogeneous terrestrial surfaces. We applied a Cluster-Tuned Matched Filter (CTMF) technique (Funk et al., 2001) to AVIRIS scenes from the COP seep field and a portion of Los Angeles known for natural CH_4 and oil seepage. The CTMF algorithm identified a number of significant CH_4 anomalies over known and probable CH_4 sources, including natural marine and terrestrial CH_4 seepage and a CH_4 plume at the Inglewood Oil Field.
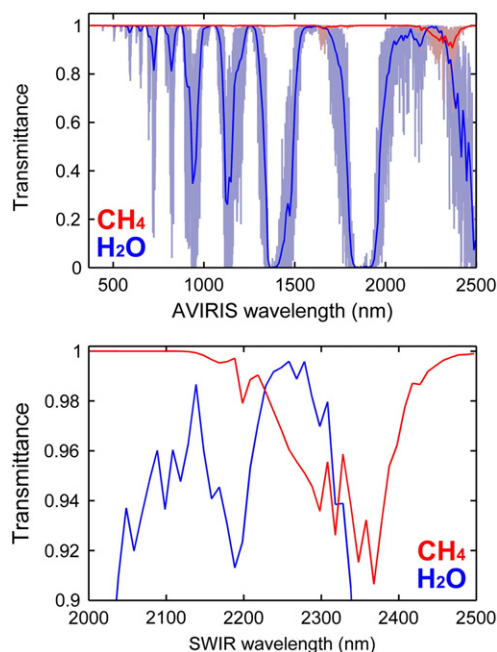

Fig. 1. (Top) CH_4 and H_2O transmittance spectra generated using Modtran 5.3, parameterized for a mid-latitude summer model atmosphere and 8.9 km sensor altitude for the COP scene. Transmittance is shown in high resolution for CH_4 (light red) and H_2O (light blue) and convolved to AVIRIS wavelengths for CH_4 (dark red) H_2O (dark blue). (Bottom) SWIR region showing considerable spectral overlap between H_2O and CH_4. (For interpretation of the references to color in this figure legend, the reader is referred to the web version of this article.)

2. Methods

2.1. Study sites

The COP seep field as well as the Mid-Wilshire and Inglewood neighborhoods of Los Angeles, California were the focus of this study because they contain known CH_4 sources from marine and terrestrial environments (Fig. 2). Located offshore of Santa Barbara, California, the COP seep field is one of the largest and best studied sources of natural CH_4 emissions. Major seeps include the Trilogy Seep, Horseshoe Seep, and IV Super Seep with bubble diameters ranging between 200 and 10^4 μm (Leifer et al., 2006a) and CH_4 fractions between 50 and 70% at the surface (Clark et al., 2010). Total atmospheric CH_4 emissions for COP are estimated at 100000 m^3/day (Hornafius et al., 1999), while the global contribution from marine seepage is estimated at 50 Tg CH_4 year^{-1} of which 30 Tg CH_4 year^{-1} reaches the atmosphere (Kvenvolden & Rogers, 2005).

The terrestrial study sites are located in Los Angeles, California, which has a history of poor air quality and CH_4 concentrations well above global averages (Townsend-Small et al., 2012). Located approximately 8 to 12 km west of downtown Los Angeles, the Mid-Wilshire and Inglewood neighborhoods have significant oil and CH_4 seepage. This is most clearly illustrated by the hydrocarbon and water mixture with visible CH_4 bubbles present at the La Brea Tar Pits. In the surrounding areas, CH_4 gas can often be seen bubbling from between cracks in paved surfaces after rains (Gurevich et al., 1993). Following the 1985 Ross Department Store explosion caused by natural CH_4 buildup, the city of Los Angeles designated a Methane Zone and Methane Buffer Zone with additional building codes requiring CH_4 mitigation such as gas detectors in addition to active and passive venting systems (Chilingar & Endres, 2005). Beyond potential safety hazards, CH_4 seepage on the global scale contributes to the estimated 20 to 40 Tg CH_4 year^{-1} released globally by natural terrestrial CH_4 seepage (Etiope et al., 2009).

The urban Los Angeles Basin contains over seventy oil fields (Chilingar & Endres, 2005) with over 21000 inactive or active oil and natural gas wells in Los Angeles county alone (DOGGR, 2010a). Much of the basin has elevated levels of CH_4, between 1.91 to 2.10 ppm based on data from four monitoring stations averaged over 1994 and 1995 (Dwight Oda, California Air Resources Board, Pers. Comm. 2010) and more recently 1.76 to 2.16 ppm in 2008 (Hsu et al., 2010). Preliminary research using stable isotope analysis suggests elevated levels of CH_4 in the Los Angeles area result primarily from non-biogenic sources such as hydrocarbon refining and gas pipelines (Townsend-Small et al., 2012). Significant diurnal variation in CH_4 concentrations has been measured and can result from transport of CH_4 enhanced air from Los Angeles to other regions of the South Coast Air Basin (Wunch et al., 2009).

Over 1700 inactive or active wells, mostly concentrated in the Salt Lake and Inglewood Oil Fields, are located in the 70 km^2 study site (DOGGR, 2010a), which was imaged by two sequential AVIRIS flights (Fig. 2a). Because many of these wells were drilled decades ago and subsequently abandoned, CH_4 leaks are well documented and primarily result from improperly sealed wells. There are an estimated 528 improperly sealed wells for the Salt Lake Oil Field alone (Pipkin & Proctor, 1992). At the Inglewood Oil Field, there is active hydrocarbon extraction, producing approximately 3.1 million barrels of oil (bbl) and 1.5 billion cubic feet (Bcf) of natural gas in 2008 (DOGGR, 2010b).

2.2. AVIRIS data

Flown on aircraft at altitudes ranging between 4 and 20 km, AVIRIS measures radiance at nadir with a spectral sampling interval and nominal Full Width Half Maximum (FWHM) of 10 nm, 34° field
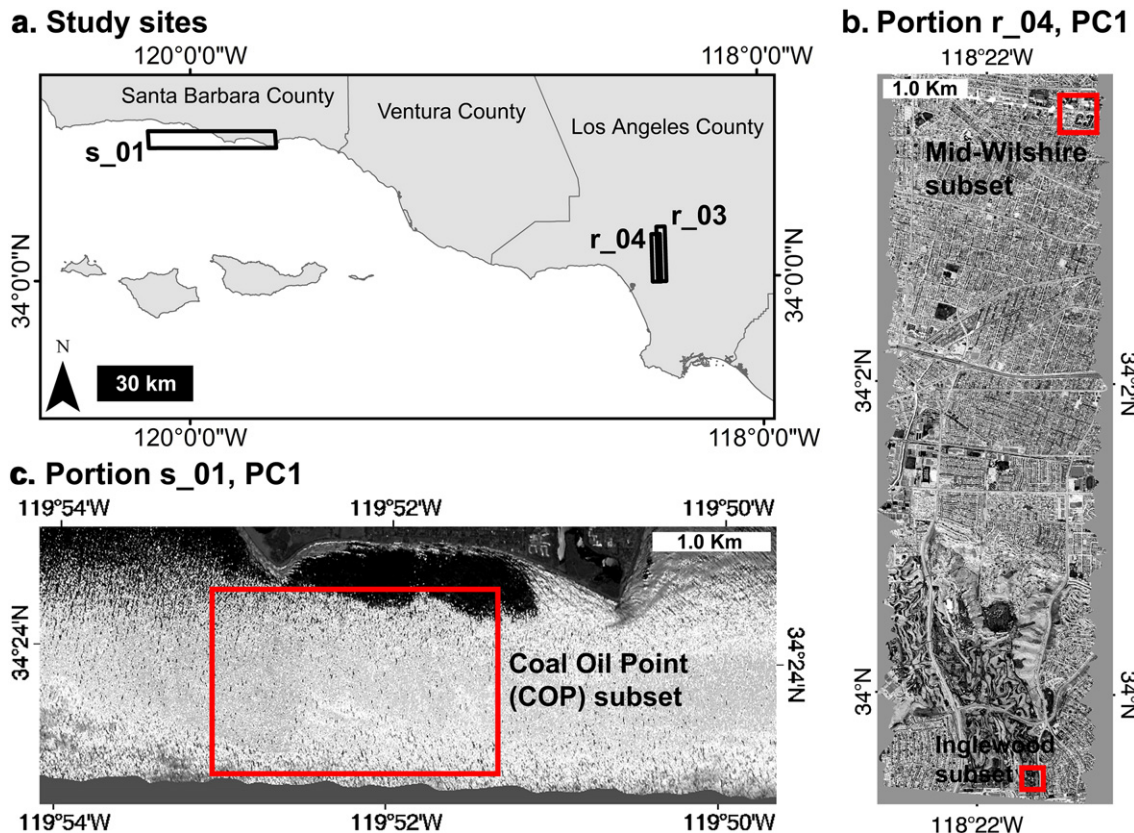

Fig. 2. (a) Study sites showing one AVIRIS scene for COP (s_01) and two overlapping flight lines (r_03, r_04) in Los Angles. (b) First principal component (PC1) for portion of r_04 showing Mid-Wilshire and Inglewood subsets. (c) PC1 for portion of s_01 showing COP subset.

of view (FOV), and 1 mrad instantaneous field of view (IFOV: Green et al., 1998). For this study, one AVIRIS scene was acquired for COP at approximately 19:55 UTC on 19 June 2008 from 8.9 km altitude (Fig. 2a, s_01), with a solar zenith of 11.4° (high sunglint), ground IFOV of ~7.5 m, and swath width of ~5.4 km. Two sequential flight lines were acquired for the Mid-Wilshire and Inglewood neighborhoods of Los Angeles between 20:57 and 21:20 UTC on 18 September 2008 from 4.0 km altitude (Fig. 2a, r_03 and r_04), with a solar zenith of 38.1°, ground IFOV of ~3 m, and swath width of ~2.7 km. AVIRIS radiance data were georectified and radiometrically calibrated by the Jet Propulsion Laboratory (JPL).

The two Los Angeles flight lines were processed to surface reflectance using a technique described by Roberts et al. (1997). This involved forward inversion to match AVIRIS radiance with modeled Modtran radiance while varying column water vapor. Column water vapor estimates were refined, averaging around 1 cm, and a ground reflectance target was used to reduce reflectance artifacts (Clark et al., 2002). In order to investigate algorithm performance, radiance and surface reflectance images were used at terrestrial locations for the CTMF analysis. For COP, the radiance image was used to avoid surface reflectance artifacts caused by low reflectance and high sunglint.

2.3. Cluster-Tuned Matched Filter

Theiler and Foy (2006) and Villeneuve et al. (1999) demonstrated that the Simple Matched Filter (SMF) and Clutter Matched Filter (CMF) could detect simulated gas plumes. To do so, a matched filter algorithm is trained with a gas target spectrum to generate a linear weighting function that produces high values when an unknown spectrum matches the shape of the gas target spectrum and is distinct from the covariance of the background. The optimal matched filter calculation uses the inverse of the scene's covariance structure to remove large-scale noise (background clutter) and to isolate the gas signal. Matched filters assume that the signal does not contribute substantially to the background scene-wide covariance. Thus, matched filters are best suited for detecting concentrated sources rather than elevated background levels present over entire scenes.

The CTMF algorithm was originally developed by Funk et al. (2001) to detect faint sulphur dioxide (SO_2) signatures superimposed on synthetic thermal images using the absorption coefficient to calculate the gas target spectrum. This study explored the use of transmittance since radiance has a linear relationship to transmittance and causes reduced radiance with increasing concentration, matching the expected impact of increased concentration in radiance space. In contrast, an increase in the absorption coefficient translates to a decrease in radiance, the opposite pattern observed in radiance space in the SWIR.

Originally developed for use with 128 spectral bands between 7.8 and 13.5 micrometers, the CTMF algorithm was modified to permit use with the 224 AVIRIS bands between 350 and 2500 nm. The CTMF was designed for weak signal detection and assumes gas plumes are modeled as a linear superposition of gas signal and background clutter as shown in the following equation (Eq. 1),

$$\mathbf{r} = \mathbf{u} - \alpha \mathbf{b} + \boldsymbol{\varepsilon} \tag{1}$$

where radiance or reflectance ($\mathbf{r}$) can be modeled as the linear combination of the mean background radiance or reflectance ($\mathbf{u}$), a gas absorption term ($-\alpha \mathbf{b}$) that reduces radiance or reflectance in the SWIR, and $\boldsymbol{\varepsilon}$, which contains both sensor noise and scene clutter. The gas absorption term contains the gas signal strength (α, a scalar representing the amount of signal present in a pixel) multiplied by the gas target spectrum ($\mathbf{b}$), which contains gas absorption features across the 224 AVIRIS bands. When applying the CTMF to AVIRIS data, atmospheric scattering can be ignored given it occurs at shorter wavelengths than gas absorptions and is usually dominated by background clutter variability.

The CTMF was applied to both radiance and reflectance images for entire AVIRIS flight lines that were first standardized by subtracting the mean and dividing by the standard deviation of the scene, both scalar values. A sample-based k-means algorithm using extreme centroid initialization was used with the first few principle components of the image to assign extreme locations for each of the k-means class centroids (Funk et al., 2001). For the Coal Oil Point and Los Angeles radiance scenes, principle components were calculated using all 224 image bands. For the Los Angeles reflectance images, principle components were calculated using 180 bands that excluded those characterized by high sensor noise or strong water vapor absorptions.

After the k-means algorithm assigns clusters and creates a k-means class image, a CTMF specifically tuned for each class was calculated. The CTMF was 'matched' to both the gas signature as well as the background clutter and was calculated using the following equation (Eq. 2),

$$\mathbf{q}_j = \frac{\mathbf{C}_j^{-1} \mathbf{b}}{\sqrt{\mathbf{b}^T \mathbf{C}_j^{-1} \mathbf{b}}} \tag{2}$$

For class j, $\mathbf{q}_j$ is the CTMF and represents an n-dimensional vector of optimal weights, where n is the number of spectral channels. $\mathbf{C}_j^{-1}$ is the inverted n by n covariance matrix for the jth class and $\mathbf{b}$ is the n-dimensional vector containing the gas target spectrum. T is the transpose operator.

Modtran 5.3 (Berk et al., 1989) was used to generate gas transmittance spectra using default gas concentrations defined by a mid-latitude summer model with 30 km visibility, 293.15 K boundary temperature, scattering turned off, and the sensor altitude for each flight line. Modtran transmittance for CH_4 and H_2O was convolved to AVIRIS wavelengths using the band centers and FWHM supplied by JPL. CH_4 and H_2O transmittance spectra indicating gas absorptions are shown in Fig. 1 for COP, including both the high resolution and convolved transmittance shown for CH_4 (red) and H_2O (blue). For the COP scene, the sensor altitude was set to 8.9 km with total column absorber amounts of 208.77 atm-cm for CO_2, 0.913 atm-cm for CH_4 and 3615.90 atm-cm for H_2O, approximately 385.01, 1.68, and 6668.34 ppmV respectively.

The sensor altitude was lower for the Los Angeles scenes (4.0 km), resulting in smaller total column absorber amounts of 117.59 atm-cm for CO_2, 0.519 atm-cm for CH_4 and 3230.10 atm-cm for H_2O. Given CO_2 and CH_4 are well mixed gasses in Modtran, the estimated 385.00 (CO_2) and 1.70 (CH_4) ppmV for the Los Angeles scenes are similar to COP, however, the higher value of 10,575.56 ppmV for H_2O results from decreased path length (lower sensor altitude) and more water vapor near the surface. Fig. 5 shows CH_4 and H_2O transmittance spectra for the Los Angeles scenes with 180 bands excluding those characterized by high sensor noise or strong water vapor absorptions that can cause reflectance artifacts.

These gas transmittance spectra were used to calculate the CH_4 and H_2O target spectrum ($\mathbf{b}$) for each scene using the following equation (Eq. 3),

$$\mathbf{b} = \mathbf{t} \; p \; s \tag{3}$$

where the n-dimensional vector $\mathbf{t}$ is the standardized gas transmittance spectrum, which is calculated by subtracting the mean of this spectrum and dividing by the standard deviation. Next, $\mathbf{t}$ is scaled by a percentage (p, gas signal percent) of the standard deviation of the image (s, a scalar value); p is chosen empirically prior to applying the CTMF algorithm (see Section 2.4). The CH_4 and H_2O target spectrum was used to generate CH_4 and H_2O CTMF results for the three AVIRIS images. Given spectral overlap between CH_4 and H_2O (Figs. 1 and 5), H_2O CTMF results were used as a means of validating CH_4 CTMF results.

In Fig. 3 (top) an example of the CH_4 target spectrum ($\mathbf{b}$) is shown calculated for the COP radiance image using p = 0.002 of the standard deviation of the image. The CTMF for class j = 1 ($\mathbf{q}_j$) is also included
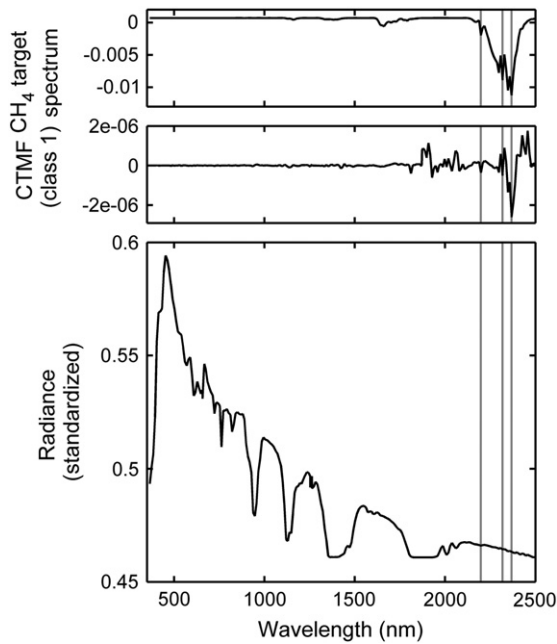
Fig. 3. (Top) CH_4 target spectrum for COP scene. (Middle) CTMF for one class. (Bottom) Standardized radiance spectrum for an ocean pixel containing sunglint within the class. Vertical lines indicate locations of strong CH_4 absorptions at 2198, 2318, and 2368 nm.

(Fig. 3, middle) with strong CH_4 absorptions indicated by vertical lines. An example of a standardized radiance spectrum for an ocean pixel containing sunglint (r_i for the ith pixel within this class) is shown in Fig. 3 (bottom).

Next, a CTMF score for ith pixel within the class (f_i) was calculated by multiplying the transpose of the CTMF (q_j) by each standardized image spectrum within the class (r_i, for radiance or reflectance), as shown in the following equation (Eq. 4),

$$\mathbf{f}_i = \mathbf{q}_j^T \ \mathbf{r}_i \tag{4}$$

Resulting from the combined operations of Eqs. (2) and (4), multiplication by the inverted covariance matrix in the numerator in Eq. (2) 'whitens' the data, removing spectral cross-correlation in the background clutter. The denominator standardizes the filter so that the CTMF image will have a variance of 1 when the signal is absent.

The CTMF score for each pixel within a class is standardized by subtracting the mean CTMF score for the class and dividing by the standard deviation of the class. This results in a mean CTMF score of 0 and standard deviation of 1 for the class; the standardization procedure continues for all j classes. Filtered pixels are then recomposed as a final output image that reduces noise and sensitivity to surface features while enhancing the gas signature.

When interpreting the CTMF image, scores greater than one indicate evidence of the gas signature, which can be quantified by the 'number of sigmas' for the z distribution. However, sigmas only can be interpreted as literal probabilities if the background clutter is Gaussian (Funk et al., 2001). Because a CTMF specifically tuned for each k-means class is used, high CTMF scores for pixels from different k-means classes that appear as contiguous pixels in CTMF images can be interpreted as highly significant. These contiguous pixels represent gas anomalies that cross over multiple land cover types and can be evaluated for consistency with known or probable emissions sources and local wind direction.

The example shown in Fig. 4 illustrates some of the challenges in detecting a gas signal over heterogeneous surfaces. For radiance or reflectance measured in two spectral bands, pixels representing the scene background clutter are shown as open circles and one pixel with gas signal added (Band 1 decrease due to absorption in this
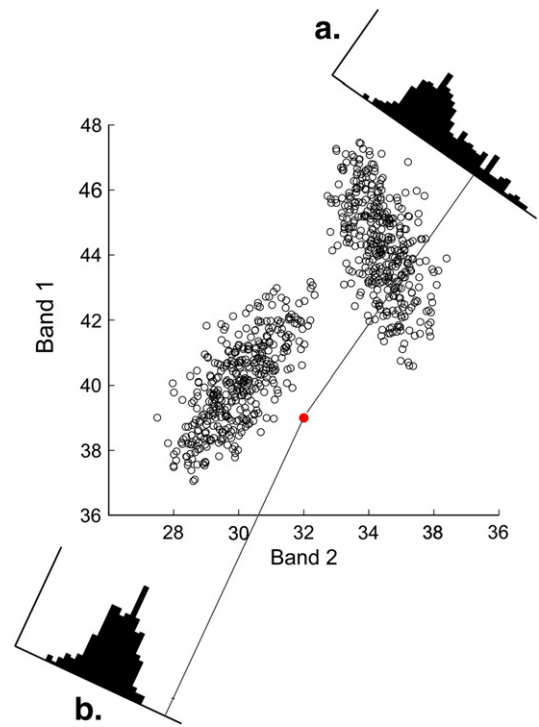

Fig. 4. For radiance (or reflectance) in two spectral channels, background clutter of the scene is shown as open circles and one pixel with gas signal added (decrease in Band 1 due to absorption) as filled red circle. (a) Projection of data cloud containing all pixels (dark and bright) by the Clutter Matched Filter (CMF) so that the pixel with the added signal will be most readily detected, but does not stand out as highly significant. (b) Projected data for only dark pixels using the Cluster-Tuned Matched Filter (CTMF) technique, resulting in the pixel with added gas signal standing out as highly significant.
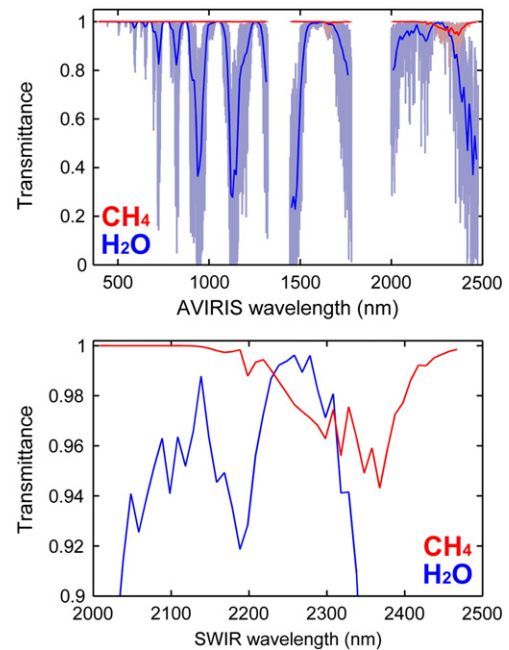

Fig. 5. (Top) CH_4 and H_2O transmittance spectra excluding bands with strong water vapor absorptions for the Los Angeles scenes generated using Modtran 5.3 parameterized for a mid-latitude summer model atmosphere and 4.0 km sensor altitude. Transmittance is shown in high resolution for CH_4 (light red) and H_2O (light blue) and convolved to AVIRIS wavelengths for CH_4 (dark red) H_2O (dark blue). (Bottom) SWIR region. (For interpretation of the references to color in this figure legend, the reader is referred to the web version of this article.)

band) is included as a filled red circle. Fig. 4a shows a projection of the data cloud containing all pixels by the Clutter Matched Filter (CMF) so that the pixel with the added gas signal will be most readily detected, but the pixel containing the gas signal does not stand out as highly significant. In Fig. 4b, the background clutter is first partitioned into two clusters consistent with two classes of surface materials, brighter pixels in the upper right and darker pixels in the lower left. The Cluster-Tuned Matched Filter (CTMF) is applied to the dark pixel cluster and the projected data for only darker pixels causes the pixel with added gas signal to stand out as highly significant. By classifying an image using k-means clustering and reducing within-class variance, a CTMF should improve performance over traditional matched filters by creating a matched filter that is specifically tuned for each cluster (Funk et al., 2001).

2.4. Input parameters for Cluster-Tuned Matched Filter

Two factors govern the performance of the CTMF — the number of clusters identified and the gas signal percent (p), which scales the gas transmittance spectrum by a percentage of the standard deviation of the image (Eq. 3). To determine an appropriate number of clusters for the k-means algorithm, a key objective is to maximize the number of clusters needed to discriminate land cover classes and reduce within-class variance, while maintaining enough pixels in each cluster to ensure adequate sample size and that the variance in the gas signal remains less than the variance of the image clusters. This is particularly important given that the CTMF calculation (Eq. 2) explicitly removes the background clutter, assuming that the gas signal is independent. In this study, the number of clusters was increased iteratively while maintaining a minimum of 1000 pixels in each cluster, resulting in 36 clusters for the entire COP scene.

For the COP scene, the CH_4 signal percent (p) was determined empirically by varying the scalar between 0.0001 and 1.00 using the 36 cluster k-means result. A visual comparison between results obtained using extreme values showed appreciable differences, but it became difficult to distinguish between the remaining results. Overall, a CH_4 signal percent of 0.002 produced anomalies that appeared the most clearly defined.

Radiance images were initially used for the Los Angeles scenes, however, CTMF anomalies were more clearly defined using the surface reflectance images due to improved classification of the heterogeneous urban environment by the k-means algorithm. For flight line r_04, k-means class images generated for different numbers of clusters were analyzed and indicated that 321 clusters maximized the number of clusters while maintaining cluster size above 1000 pixels for the surface reflectance image. The CH_4 signal percent was varied between 0.0001 and 1.00, but identifying the optimal result remained challenging so 0.002 was used for consistency with the COP example.

2.5. Segmentation and classification

In order to reduce noise and isolate contiguous pixels with high CTMF scores, a segmentation approach based on 8-connectivity was used by defining a score threshold and minimum number of pixels for the segments. An iterative process was used to determine the appropriate threshold and minimum population that preserved regions of contiguous pixels without resulting in too many small segments. Next, a mask of the segments was applied to the reflectance scene, resulting in an image that contained reflectance spectra only for segmented regions.

To distinguish true CH_4 anomalies from false positives, reflectance spectra from the segmented regions were classified using MESMA (Multiple-Endmember Spectral Mixture Analysis: Roberts et al., 1998). MESMA is particularly well suited for the spectral diversity of urban environments because it permits the number and types of endmembers to vary on a per-pixel basis (Roberts et al., 2012). 'Viper-tools,' an ENVI add-

on (www.vipertools.org), was used to generate the spectral library that was used in the classification.

A spectral library was generated from endmembers obtained in the field using an Analytical Spectral Device (ASD Inc., Boulder, Colorado) full range spectrometer that samples between 350 and 2500 nm and image endmembers from the AVIRIS scene. The Endmember Average Root Mean Square Error (EAR) method was utilized to optimize the endmembers for the spectral library by creating the smallest number of spectra for each land cover class while maximizing the separation between surfaces (Dennison & Roberts, 2003). EAR uses MESMA to calculate the average error for a given endmember in modeling spectra within a land cover class; endmembers with lower within class average root mean square error (RMSE) are representative endmembers for a given land cover class. Endmembers were organized into two MESMA classes: surfaces prone to false positives (confusers) and probable CH_4 anomalies. These endmembers were used to unmix the segmented reflectance image and generate a classification image indicating which anomalies are probable CH_4 anomalies or likely false positives.

3. Results

3.1. Cluster-Tuned Matched Filter

3.1.1. Coal Oil Point

CTMF results obtained using 36 clusters and a CH_4 signal percent of 0.002 produced anomalies with a maximum CTMF score of 43.8 (positive values as CH_4 anomalies), minimum of −48.5, mean of 0.0, and standard deviation of 1.0 for the entire COP radiance image. A subset of CTMF results is shown in Fig. 6d for a region of high sunglint as well as dark ocean pixels, with a maximum radiance measured in $uWcm^{-2} sr^{-1} nm^{-1}$ at 2100 nm of 6.466 (sensor saturation), minimum of 0.026 (0% reflectance), and mean of 2.779 (95.7% reflectance) within the image subset. In Fig. 6d, high CTMF scores represent large sigma values that indicate rotated pixels that are far from the expected value of 0 (Fig. 4b) and are very likely to contain elevated CH_4 concentrations. Bright pixels clearly indicate positive CH_4 anomalies consistent with a southwesterly wind measured at the nearby West Campus Station (2.3 m s^{-1} from 236°).

These anomalies emanate from known seeps, including the Trilogy Seep (TRI), IV Super Seep (IV), and Horseshoe Seep (HS), as shown by sonar return contours of subsurface bubble plumes in Fig. 6a (Leifer et al., 2010). These CH_4 anomalies also closely resemble results obtained using the AVIRIS CH_4 index, ζ (L_{2298} / L_{2058}), developed by Bradley et al. (2011). In Fig. 6b, AVIRIS CH_4 index results for the same region are shown, with elevated CH_4 indicated by lower values (dark pixels) caused by reduced radiance in the numerator (L_{2298}) due to increased absorption by CH_4 relative to CO_2 absorptions (L_{2058}). In Fig. 6c, CTMF results for water vapor show no H_2O anomalies, indicating the anomalies present in Fig. 6d are due to CH_4. Using visual assessment, we verified that CH_4 anomalies were not present in any of the principal components of the AVIRIS scene and have included the first principal component of the subset in Fig. 6a.

3.1.2. Los Angeles

For the entire reflectance scene for flight line r_04, the CTMF image had a maximum score of 17.0, minimum of -17.0, mean of 0.0, and standard deviation of 1.0. The CTMF algorithm was also applied to scene r_03 using input parameters previously defined for r_04, resulting in a maximum score of 16.9 and minimum of −13.8. CTMF results indicate a number of well defined CH_4 anomalies coinciding with locations of known or probable CH_4 emission sources. For the overlapping portion of scene r_03 and r_04 (Fig. 2), the location of well defined CH_4 anomalies remained consistent in CTMF results from either scene. Visual assessment was used to verify that CH_4 anomalies were not present in principal components of the scene and results compared with CTMF results for water vapor as an additional means of validation.
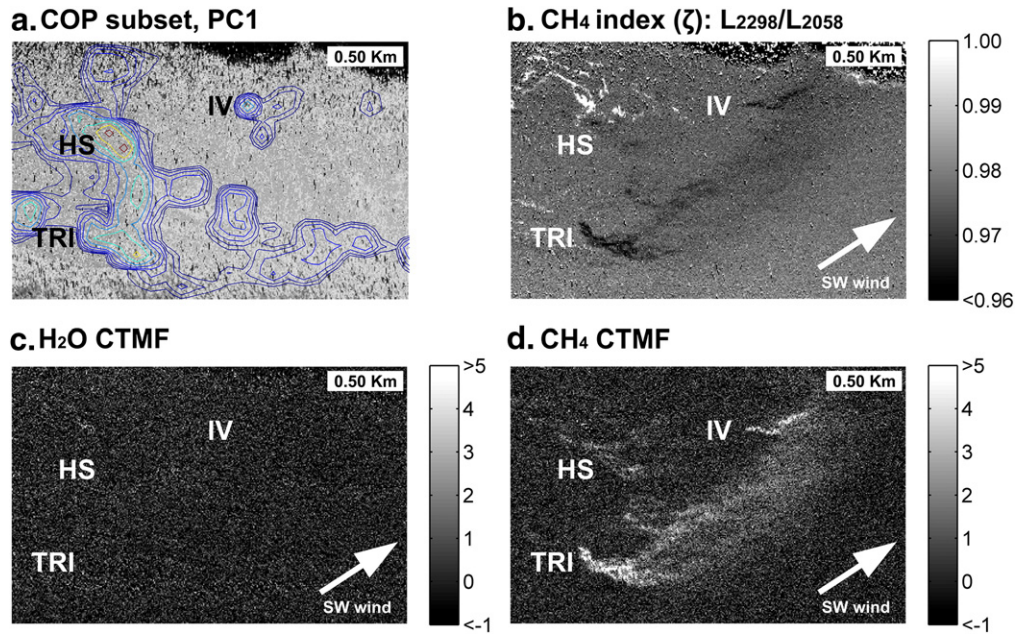
a. COP subset, PC1

b. CH₄ index (ζ): L₂₂₉₈/L₂₀₅₈

c. H₂O CTMF

d. CH₄ CTMF

Fig. 6. (a) PC1 for COP subset shown in Fig. 2c overlain with sonar contours (Leifer et al., 2010) indicating known seeps, including the Trilogy Seep (TRI), IV Super Seep (IV), and Horseshoe Seep (HS). (b) AVIRIS CH₄ index, ζ (L₂₂₉₈ / L₂₀₅₈), indicating elevated CH₄ (dark pixels) corresponding with known seep locations. (c) For the same region, CTMF results for water vapor show no H₂O anomalies. (d) CTMF results for CH₄ with positive values denoting CH₄ anomalies (bright pixels) consistent with results obtained using CH₄ index.

For this study we focus on image subsets containing the most prominent anomalies located at the Inglewood Oil Field and near the La Brea Tar Pits.

The first area of interest is located at the southern edge of the Inglewood Oil Field (Fig. 2b, Inglewood subset). For scene r_04, the true color subset shown in Fig. 7a has a maximum surface reflectance of 47.6%, minimum of 3.3%, and mean of 26.7% measured at 2100 nm. For the same region, a plume-like feature is clearly visible in the CTMF result for CH₄ (Fig. 7e) while the k-means class image (Fig. 7b) indicates that the anomalies cross over multiple classes and thus different land cover types, including soil as well as green and non-photosynthetic vegetation. This is more clearly emphasized in Fig. 7c, where the
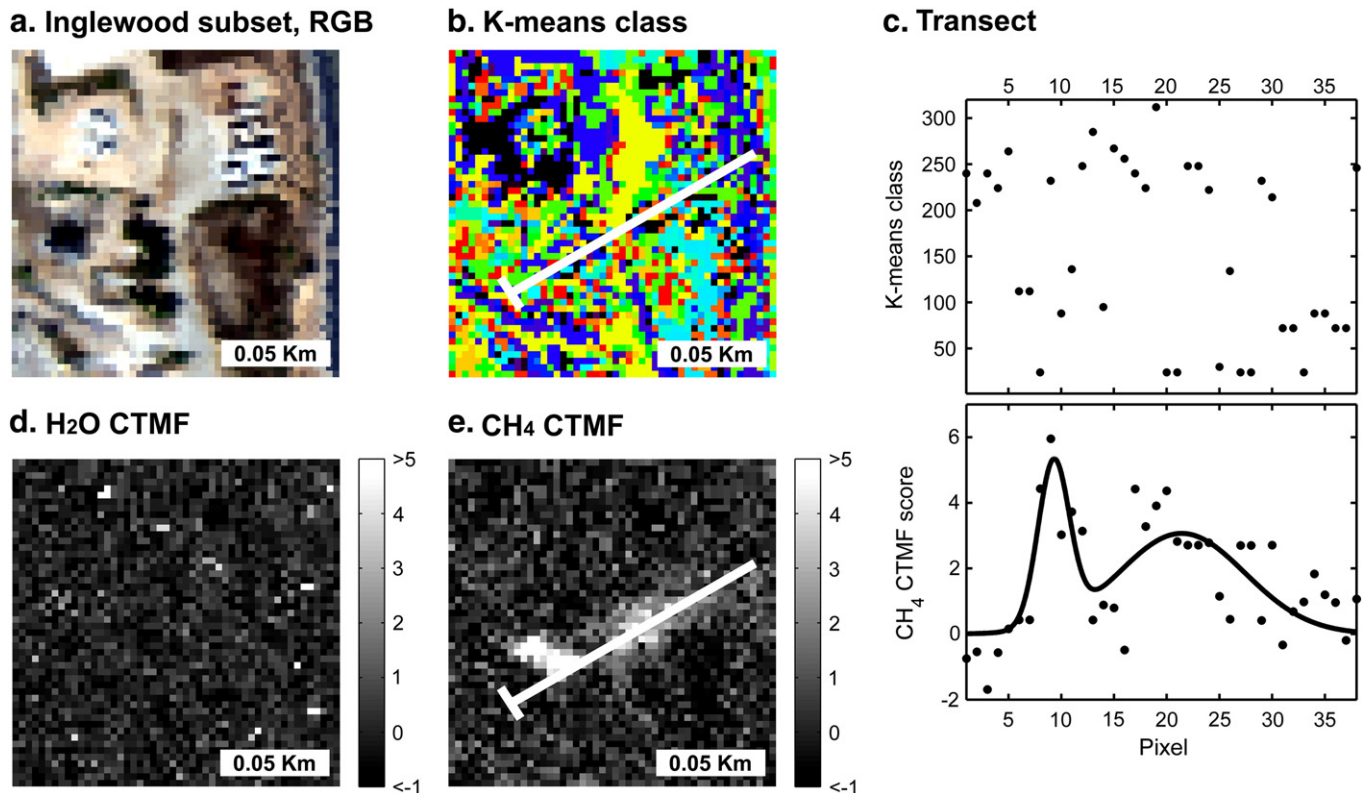
a. Inglewood subset, RGB

b. K-means class

c. Transect

d. H₂O CTMF

e. CH₄ CTMF

Fig. 7. (a) Inglewood subset shown in true color (RGB) for flight line r_04. (b) For the same region, k-means class image indicates numerous land cover classes. (c) Along transects shown in b and e, the class and CH₄ CTMF score for each pixel is shown, indicating that the CH₄ anomalies cross over multiple land cover classes. (d) CTMF results for water vapor show no H₂O anomalies. (e) CTMF results for CH₄ with positive values denoting CH₄ anomalies (bright pixels).

k-means class is plotted for each pixel along the transect shown in Fig. 7b. For the same transect shown in Fig. 7e, the CH₄ CTMF results are best fit using a robust Gaussian curve (Matlab Curve Fitting Toolbox, Mathworks, Natick, Massachusetts). CTMF results for H₂O are shown in Fig. 7d and indicate no H₂O anomalies in the image subset.

Two AVIRIS flight lines were acquired over this location approximately 6.5 min apart and CH₄ anomalies clearly change between the earlier scene, r_03 (Fig. 8b), and the later scene, r_04 (Fig. 8d). For presentation, CTMF results are provided for both scenes using a median filter with a 2 by 2 pixel kernel (Fig. 8b and d, left), while the original results are displayed with identical transects (T1 and T2 in Fig. 8b and d, right). To compare changes in the anomalies between scenes, CH₄ CTMF results for transects were best fit using robust Gaussian curves. Transect 1 (T1 in Fig. 8c) crosses a portion of the scene with the highest CTMF scores and comparison of best fit curves indicates the anomalies in the later scene (r_04) exhibits a greater amplitude and extent ($R^2 = 0.89$, RMSE = 1.10) than r_03 ($R^2 = 0.78$, RMSE = 0.89).

In Fig. 8d, Transect 2 (T2) first crosses over the southern edge of the observed CH₄ anomalies, next a stand of trees, and finally a region where CTMF scores appear to gradually decrease. Fig. 8e shows a second order fit for Transect 2 of r_04 ($R^2 = 0.54$, RMSE = 1.30), with values greatest towards the southwest, markedly decreasing in the vicinity of the trees, and gradually decreasing to the northeast. This is consistent with local meteorological data indicating a 2.2 m s^{-1} southwesterly wind at the time of image acquisition (weatherunderground.com, 2012). It is unclear whether the trees are obscuring the CH₄ signal due to liquid water absorption and low reflectance in the SWIR, or if the spatial patterns are the result of an intermittent release. Transect 2 for r_03 was modeled with a first order Gaussian fit ($R^2 = 0.54$, RMSE = 0.88), clearly indicating significant change in the plume profile during the 6.5 min between the two flight lines. This is consistent with a gas plume rather than a stationary surface material causing a false positive. Google Earth imagery from 14 November 2009, acquired one year after the AVIRIS flights, was used to resolve surface features, including what appears to be two hydrocarbon

storage tanks located immediately upwind of the anomalies (Location L1 in Fig. 8a: Google Earth, 2012). Given the CH₄ plume is likely near the surface, the changing appearance between scenes cannot be explained by differing view geometries, which would cause a small spatial shift rather than a significant change in the shape of the anomalies.

Eight kilometers north of the Inglewood subset, several CH₄ anomalies are observed in the region surrounding the La Brea Tar Pits (Fig. 2b, Mid-Wilshire subset). A subset of the scene is shown in Fig. 9a, with a maximum surface reflectance of 53.8%, minimum of 0.3%, and mean of 14.1% measured at 2100 nm within the image subset. Prominent CH₄ anomalies are visible on the eastern edge of the La Brea Tar Pits, a hydrocarbon and water mixture known to produce large CH₄ bubbles tens of centimeters in diameter (Fig. 9e, Location L1). On the opposite corner of Wilshire Boulevard and Curson Avenue, CH₄ anomalies are located in a courtyard bounded by two multi-story office buildings (Fig. 9e, Location L2). These buildings are documented as continuously venting CH₄ (Chilingar & Endres, 2005). The CH₄ appears to accumulate in the courtyard, where it would be almost completely surrounded by the six-story office complex. These anomalies extend through the north entrance of the courtyard, remain faintly visible immediately north of the office complex, and are consistent with CH₄ advection by south-westerly winds.

Closer inspection of CH₄ CTMF results indicates the courtyard anomalies cross over multiple k-means classes (Fig. 9b), including impervious and green vegetation land cover types. This is clearly indicated in Fig. 9c by comparing the k-means class for each pixel along the transect shown in Fig. 9b. CH₄ CTMF scores for the same transect are also shown and indicate elevated values to the northeast. While prominent CH₄ anomalies are located at a known source at the La Brea Tar Pits and probable region of elevated CH₄ in the courtyard, CTMF results for water vapor do not indicate H₂O anomalies at these locations (Fig. 9d).

Continuous air samples were collected between 3:00 and 4:00 LT on 22 February 2012 using a cavity ring-down greenhouse gas sensor (G2301, Picarro, Santa Clara, California: Farrell et al., 2013) to
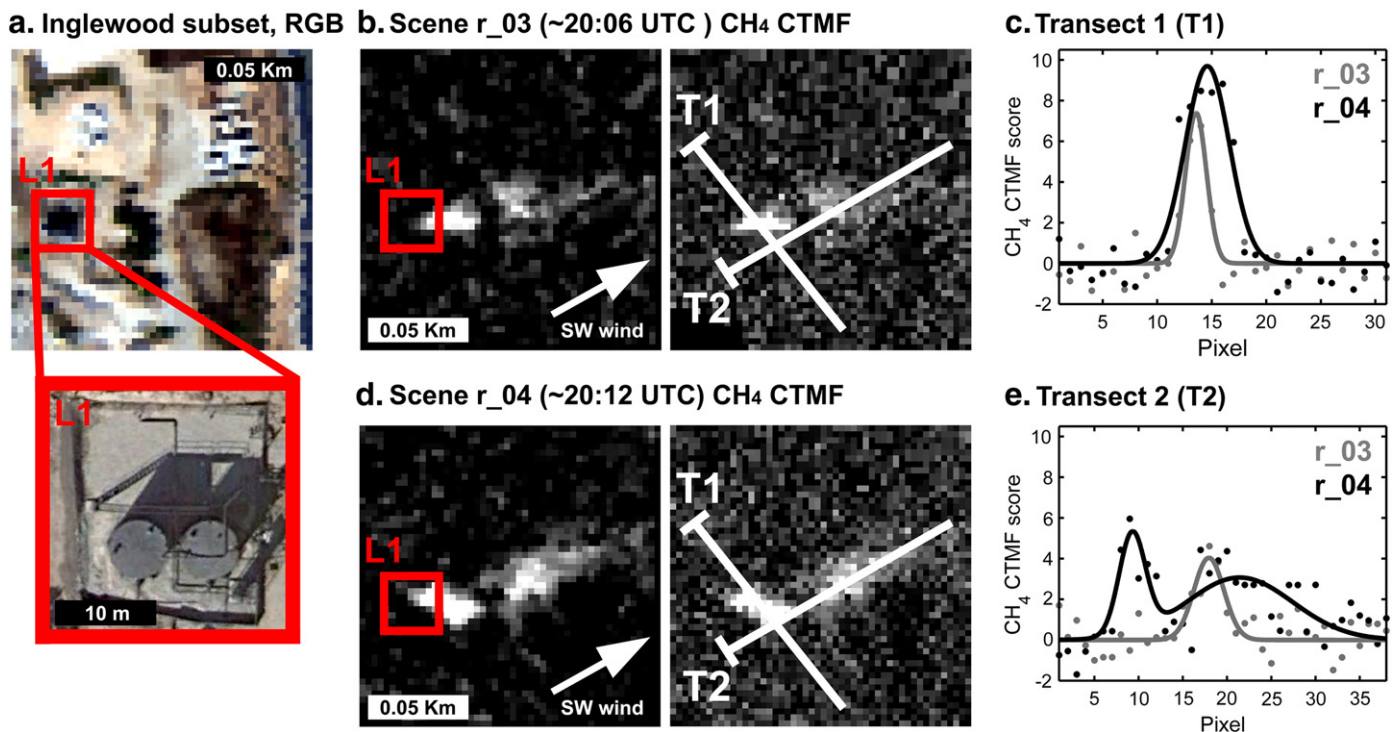

Fig. 8. (a) Inglewood subset shown in true color with close-up of hydrocarbon storage tanks (Location L1) from 14 Nov. 2009 (Google Earth, 2012). (b) CTMF results for CH₄ with positive values denoting CH₄ anomalies for flight line r_03. Left, using median filter with 2 by 2 pixel kernel and on right, original results. (d) CTMF results for r_04. For r_03 and r_04, identical transects are shown on the right. (c) Results for Transect 1 (T1) were best fit using robust 1st order Gaussian curves. (e) Transect 2 (T2) varies significantly between r_03, with 1st order fit, and r_04, with a 2nd order Gaussian fit.
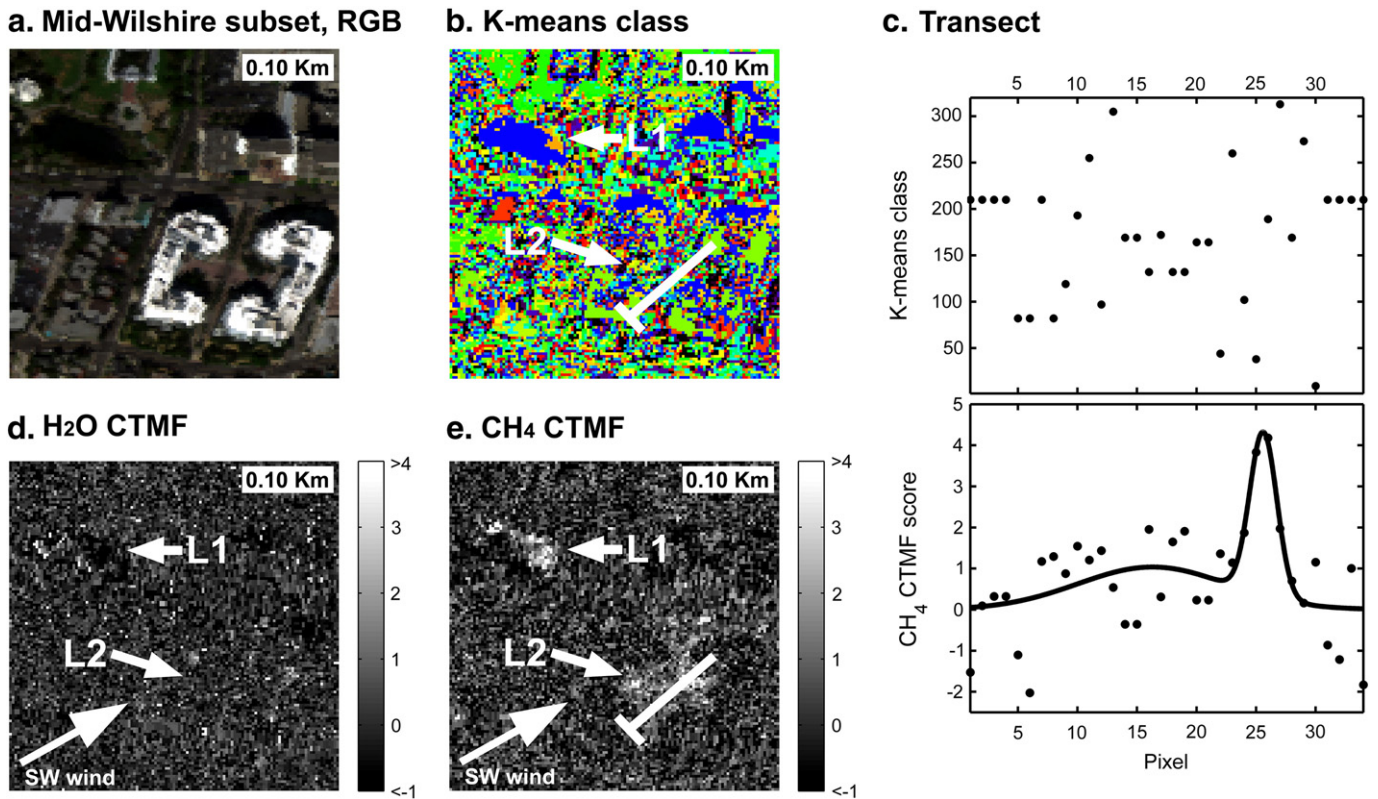
a. Mid-Wilshire subset, RGB

b. K-means class

c. Transect

d. H2O CTMF

e. CH4 CTMF

Fig. 9. (a) Mid-Wilshire subset for flight line r_04 shown in true color. (b) For the same region, the k-means class image indicates numerous land cover classes. (c) Along transects shown in b and e, the class and CTMF score for each pixel is shown, indicating that the CH_4 anomalies cross over multiple land cover classes. (d) CTMF results for water vapor show no H_2O anomalies. (e) CTMF results for same area with positive values denoting CH_4 anomalies. Location 1 (L1) indicates eastern edge of La Brea Tar Pits, a known CH_4 source, and Location 2 (L2) a courtyard bounded by a multi-story office complex with continuous CH_4 venting.

characterize CH_4 emissions for the region surrounding the La Brea Tar Pits. In Fig. 10, CH_4 measurements are shown for a region similar to the Mid-Wilshire subset shown in Fig. 9, with concentrations between 3.066 ppm and 45.508 ppm with a mean of 6.44 ppm. Winds were calm at the time of sampling and measurements near the courtyard's south entrance show an approximately Gaussian shape with a 45.508 ppm maximum. This is consistent with CH_4 accumulating in the courtyard from continuous CH_4 venting by the office complex and escaping through the courtyard's south entrance. These results can be compared with CH_4 anomalies shown in Fig. 9e that extend through the courtyard's north entrance and are consistent with CH_4 advection
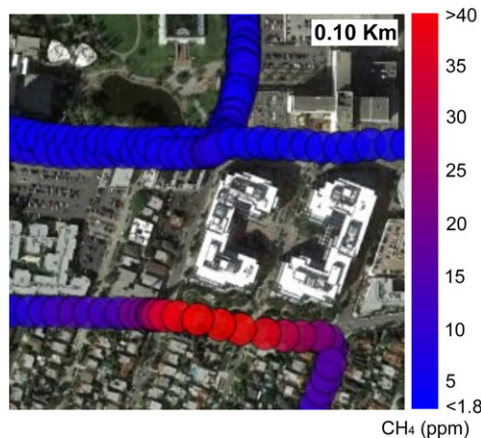

Fig. 10. In situ CH_4 measurements near the La Brea Tar Pits (2 s time average) indicate concentrations between 3.066 and 45.508 ppm for this scene subset (Google Earth, 2012). A pronounced increase in concentration occurs immediately south of the office complex with peak measurements near the south entrance of the courtyard.

by 2.2 m s^{-1} southwesterly winds when the AVIRIS image was acquired on 18 September 2008.

3.2. Noise and false positives

CTMF results consistently appear noisy and attempts to reduce 'speckle' by varying input parameters, such as the number of clusters and CH_4 signal percent, were largely unsuccessful. As a means of optimizing results, Moran's Spatial Statistics were used to assess local homogeneity (Cliff & Ord, 1981), but values remained nearly identical despite varying both the number of clusters and the CH_4 signal percent. The Moran's index appears primarily influenced by noise and false positives present in CTMF results, rather than subtle variations in CH_4 anomalies.

Although well defined anomalies located at and downwind from known or probable CH_4 sources were identified, apparent false positives also occurred and result from surfaces with strong absorptions at the same wavelengths as CH_4. In Fig. 11, reflectance spectra for surfaces prone to false positives (confusers) are shown (Spectra S2 through S11) indicating SWIR absorptions consistent with those present in CH_4 transmittance spectrum S1. Confusers included oil-based paints (S2 through S6) and a number of roofs exhibiting a strong absorption feature for calcite (CO_3) at 2338 (Fig. 11, S7).

Apparent false positives generally appeared as contiguous pixels with a shape that mimics an underlying surface feature, for example individual rooftops within CH_4 CTMF results. This suggests that the AVIRIS spectral resolution limits the ability of the CTMF algorithm to accurately resolve between a pure CH_4 signature and land cover types with strong absorption features between 2200 and 2500 nm. Despite this, the percentage of pixels within each k-means class exhibiting high CTMF scores remained small across classes, for example 0.01 to 1.27% of pixels within each class exhibited scores greater than 3
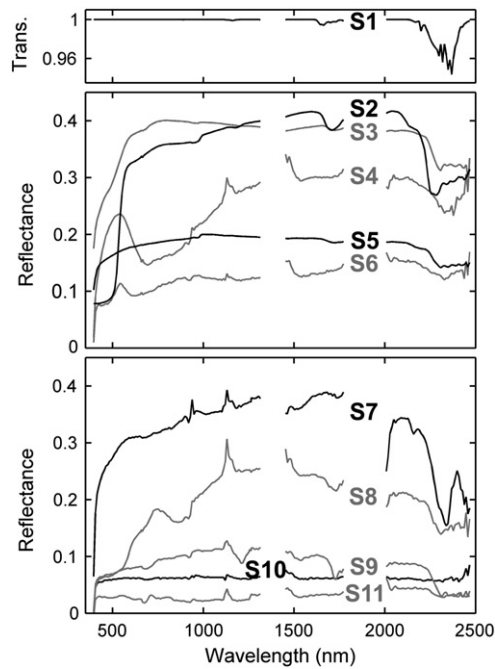
Fig. 11. Reflectance spectra for surfaces prone to false positives (confusers) are shown (Spectra S2 through S11) indicating absorptions consistent with those present in CH_4 transmittance spectrum S1. Absorptions between 2048 and 2467 nm for oil-based paints (S2 through S6) and at 2338 nm for calcite (S7) explain false positive characterization.

for Los Angeles scene r_04. One class containing shade pixels had a higher value of 2.40% suggesting a slight bias towards dark surfaces, however no systematic bias towards the remaining classes was observed.

3.3. Segmentation and classification

In order to reduce noise and isolate CH_4 anomalies for Los Angeles scene r_04, segmentation using a CTMF score threshold greater than 1.5 and minimum population size of 55 pixels (~500 m²) resulted in 16 segments totaling 1331 pixels (0.04% of the original pixels within the AVIRIS scene). To distinguish true CH_4 anomalies from false positives, reflectance spectra from the segmented regions were classified using MESMA. From a spectral library containing 1089 field spectra obtained between 23 May and 25 June 2001 for the Santa Barbara urban area (Herold et al., 2004), spectra with the lowest 2 or 3 EAR scores for each of the 58 land cover classes were selected. The resulting 164 field spectra then were used to unmix the segmented reflectance scene using a two endmember model consisting of a bright endmember and photometric (spectrally flat) shade, fractional constraints between 0 and 100%, and a root mean square error (RMSE) constraint below 5.0%.

Portions of the segmented reflectance image remained unclassified, so image endmembers were used to supplement the spectral library. Regions of interest (ROIs) were created in the original reflectance image and located outside those areas defined by the segmented reflectance image. For each ROI, the spectrum with the lowest EAR was added to the spectral library as an image endmember. In a few instances, appropriate endmembers could not be found outside of segmented regions so spectra obtained within segments were used. For example, accurate classification of the hydrocarbon and water mixture of the La Brea Tar Pits (Fig. 11, S11) only was possible by choosing endmembers at this location. Similarly, image endmembers were selected for suspected false positives caused by three surfaces of unknown composition with strong absorptions in the SWIR: a blue awning (likely a painted metal surface), a running track (likely a rubberized material), and what appears to be plastic sheeting used as an erosion barrier (Fig. 11, S4, S8, and S9 respectively).

These field spectra and image endmembers then were organized into two MESMA classes: confusers and probable CH_4 anomalies. A complete list of land cover categories for either class is shown in Table 1, with surfaces prone to false positives (confusers) including oil-based paints, calcite, and surfaces of unknown composition (blue awning, running track, and erosion barrier). Fresh asphalt is another likely confuser, with possible hydrocarbon absorptions in the SWIR resulting from tar. Therefore, the La Brea Tar Pits, a hydrocarbon and water mixture with fresh tar visible on the surface, was included as a potential confuser. The remaining land cover categories were included in the probable CH_4 anomalies class and made up of impervious surfaces not prone to false positives, green and non-photosynthetic vegetation, and soils.

These spectra were then used to unmix the segmented reflectance image resulting in a classification using 109 successful models. Field spectra and image endmembers that modeled only a small portion of the scene were removed, reducing the library to 93 spectra. This final spectral library was used to unmix the scene and generated a classification image with 0 unclassified pixels.

The classification of the segmented reflectance image for the Inglewood subset is shown in Fig. 12b, with confusers indicated in red and probable CH_4 anomalies in green. This region is composed of surfaces that make up the probable CH_4 anomalies class, including soil as well as green and non-photosynthetic vegetation, while no confusers were detected. In Fig. 12c, CH_4 CTMF scores are displayed with highest scores in orange (greater than 3.5), intermediate values as yellow (2.5 to 3.5), and low scores in cyan (1.5 to 2.5). This indicates true CH_4 anomalies consistent with southwesterly winds and emission from or near the hydrocarbon storage tanks located at L1 in Fig. 8a. For reference, the original reflectance image for the same subset is included in Fig. 12a. For the segmented portion shown in Fig. 12c, surface reflectance measured at 2100 nm had a maximum of 41.6%, minimum of 3.9%, and mean of 25.2%.

To classify the La Brea Tar Pits, it was necessary to select image endmembers directly from this location, which were included in the confusers class due to the presence of oil and tar. As a result, the anomalies at the eastern edge of the La Brea Tar Pits mostly are classified as confusers (Fig. 12e). Oil and fresh tar have SWIR absorption features that could cause false positives in CTMF results, however, CH_4 bubbles tens of centimeters in diameter also are present at this location. Accordingly, these anomalies are likely caused by combined absorption features resulting from CH_4 gas and liquid hydrocarbons.

Most of the courtyard anomalies appear as the probable CH_4 anomalies class and mainly include impervious surfaces like brick and pavement as well as green vegetation (Fig. 12e). However, confusers do exist along the edge of the heavily shaded portion of the courtyard, including calcite, asphalt, as well as green and white paint endmembers.

Table 1
Classification results of segmented reflectance image for flight line r_04 indicating land cover categories for two MESMA classes: probable CH4 anomalies and confusers.

| MESMA class	Land cover categories	Number pixels	Percent in segmented image
Probable CH4 anomalies	Impervious (concrete, brick, tile, etc.)	460	34.56
	Non-photosynthetic vegetation	187	14.05
	Green vegetation	170	12.77
	Soil	95	7.14
Confusers	Unknown composition	186	13.97
	Hydrocarbon/water mixture	102	7.66
	Oil-based paints	80	6.01
	Calcite	44	3.31
	Asphalt	7	0.53
Unclassified pixels		0	0.00
Total pixels in segmented image		1331	100.00
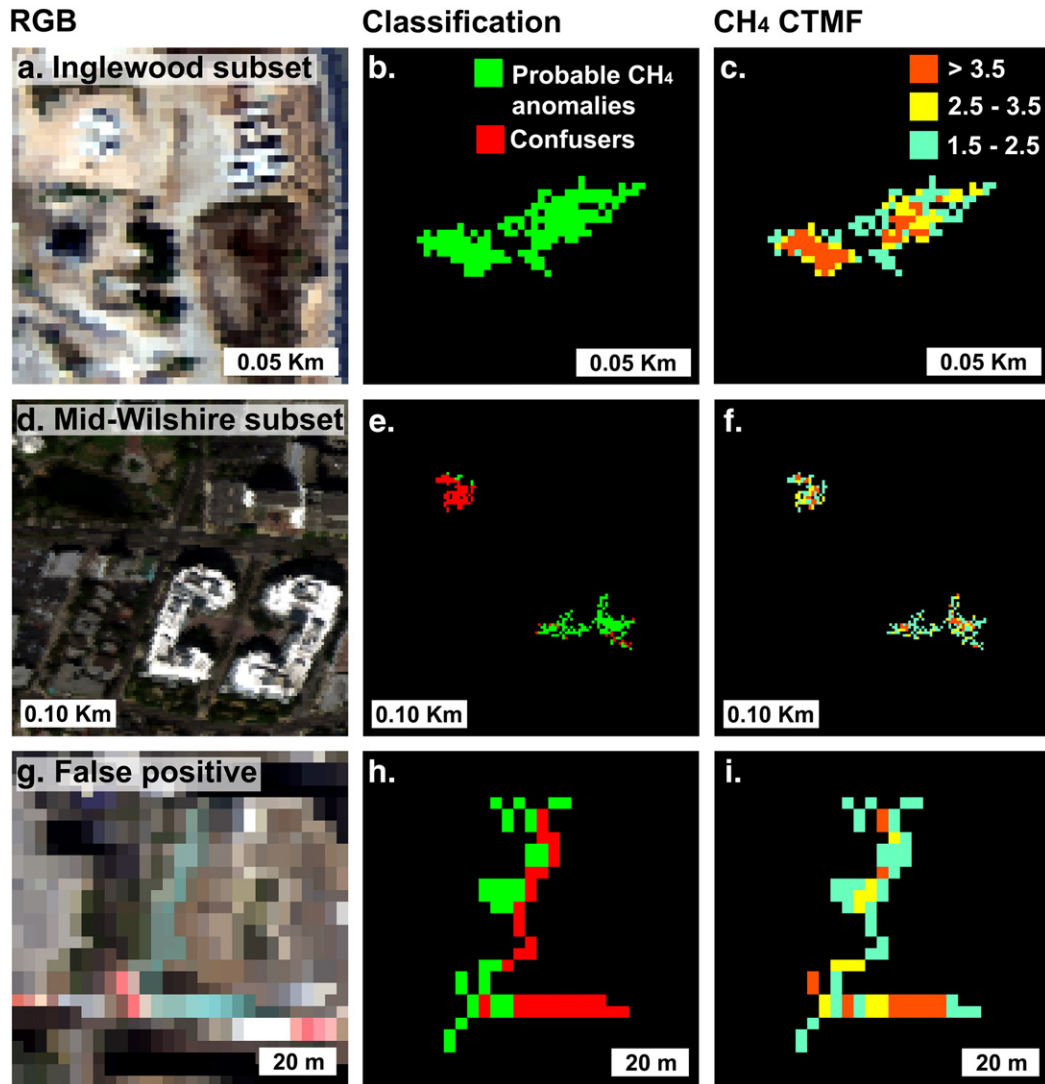
Fig. 12. True color subsets, classification results of segmented reflectance images, and CH₄ CTMF scores are displayed for flight line r_04. (a, b, c) Inglewood subset. (d, e, f) Mid-Wilshire subset. (g, h, i) Subset with contiguous pixels classified as endmembers from the confusers class, indicating segment is a likely false positive.

Because the classification was limited to two endmember models, these are likely the result of mixed pixels that were misclassified as confusers. Therefore, elevated CH₄ CTMF scores in the courtyard likely represent true CH₄ anomalies and are consistent with continuous CH₄ venting by the surrounding office complex and the very elevated CH₄ concentrations up to 45.508 ppm measured at the south courtyard entrance.

For the segmented portion shown in Fig. 12f, surface reflectance had a maximum of 31.6%, minimum of 0.4%, and mean of 8.9% measured at 2100 nm. Most of the anomalies at the La Brea Tar Pits occur for dark spectra (around 5% reflectance at 2100 nm) compared to the considerably brighter surfaces that make up the courtyard. Therefore, the CTMF technique is capable of detecting CH₄ anomalies across a wide range of surface reflectance.

Fig. 12h provides the classification result for an image subset located approximately 1.0 km north of the La Brea Tar Pits. The confusers classification includes contiguous pixels corresponding to the blue awning in Fig. 12g, which likely is a painted metal surface with strong SWIR absorptions (Fig. 11, S4). In this example, it appears that many pixels classified as probable CH₄ anomalies may result from poor modeling of mixed pixels using two endmember models. Examining reflectance spectra adjacent to pixels classified as confusers reveals strong absorption features similar to those present in the confusers pixels. This is consistent with an edge effect caused by mixed pixels and indicates

this segment is a likely false positive. In a different location, a similar edge effect was observed for mixed asphalt pixels, which systematically exhibited high CH₄ CTMF scores.

A summary of classification results of the segmented reflectance image r_04 are presented in Table 1. For the probable CH₄ anomalies class, the impervious land cover category made up 460 pixels (34.56%) of the total 1331 pixels within the segmented scene, followed by non-photosynthetic vegetation (14.05%), green vegetation (12.77%), and soil (7.14%). For the confusers class, 13.97% of the scene was of unknown composition and classified using image endmembers from the blue awning, running track, and erosion barrier. Image endmembers from the hydrocarbon/water mixture were used to classify the La Brea Tar Pits (7.66% of the scene), while the remaining land cover categories for the confusers class included oil-based paints (6.01%), calcite (3.31%), and asphalt (0.53%). Of the total 1331 pixels within the segmented scene, 68.52% of pixels were classified as endmembers corresponding to the probable CH₄ anomalies class and 31.48% as the confusers class.

4. Discussion

The observed CH₄ anomalies for COP and the Mid-Wilshire neighborhood of Los Angeles suggest significant natural CH₄ seepage in these regions. COP is one of the largest natural marine seeps in the world, with

total atmospheric CH_4 emissions estimated at 100000 m³/day (Hornafius et al., 1999). The Mid-Wilshire area has well documented CH_4 seepage, including CH_4 bubbles in the La Brea Tar Pits, CH_4 gas bubbling from between cracks in paved surfaces after rains (Gurevich et al., 1993), and additional building codes requiring CH_4 mitigation such as gas detectors in addition to active and passive venting systems (Chilingar & Endres, 2005). The CTMF technique shows promise for detecting CH_4 from natural geological seepage, which contributes an estimated 30 Tg CH_4 year⁻¹ globally to the atmosphere from marine seepage (Kvenvolden & Rogers, 2005) and between 20 and 40 Tg CH_4 year⁻¹ for natural terrestrial seepage (Etiope et al., 2009).

The CTMF approach also demonstrates potential for detection of fugitive CH_4 emissions, a term describing largely unmonitored CH_4 releases associated with petroleum production and industrial processes that are poorly constrained (Howarth et al., 2011). CH_4 anomalies consistent with fugitive emissions were detected at the Inglewood Oil Field immediately downwind of two hydrocarbon storage tanks. Storage tanks are a major source of CH_4, emitting an estimated 212 Gg for the United States in 2009 (EPA, 2011). North American natural gas storage tanks have an emission factor of between 4.3 and 42.0×10^{-4} Gg CH_4 per (10^6) m³ gas withdrawals per year (IPCC, 2000) and condensate tank batteries have been documented to emit between 141 and 14158 m³ natural gas and light hydrocarbon vapors each day (EPA, 2010).

For the Los Angeles Basin, CH_4 emissions are poorly constrained and statewide inventories appear to underestimate urban CH_4 emissions (Wunch et al., 2009). Natural CH_4 seepage is well documented in this region (Chilingar & Endres, 2005) and there are a number of potential sources of fugitive emissions. These include natural gas pipelines, the Inglewood Gas Plant, improperly sealed wells (Pipkin & Proctor, 1992), the Playa del Rey Oil Field which is currently being used for natural gas storage (Chilingar & Endres, 2005), as well as a number of refineries in the El Segundo neighborhood and near the Port of Long Beach. Isotopic analysis by Townsend-Small et al. (2012) indicates the majority of CH_4 emissions in Los Angeles are from fossil fuel sources, including natural seepage from geological formations as well as fugitive emissions. Therefore, the combination of airborne imaging spectrometry and the CTMF technique offers the potential to detect concentrated natural and fugitive emissions in areas where sources may be unknown or poorly quantified.

Significant CH_4 sources have been documented by Farrell et al. (2013) across much of the Los Angeles Basin, while the lowest values were located in the coastal Rancho Palos Verde area (1.993 ppm) and at the base of the San Bernadino Mountains. All concentrations in the Los Angeles Basin were elevated compared to the Mojave Desert, where average values were 1.860 ppm. Particularly high concentrations were observed near the La Brea Tar Pits (45.508 ppm), Marina del Rey (4.740 ppm), and at the Port of Long Beach (3.676 ppm) near a number of hydrocarbon storage tanks. These high concentrations suggest that unaccounted natural CH_4 seepage and fugitive emissions in the 'bottom-up' California Air Resources Board (CARB) emissions inventory might explain some of the discrepancy between the CARB estimate of 3.0 MMT CO_2 E year⁻¹ and the 'top-down' estimate of 4.2 MMT CO_2 E year⁻¹ by Hsu et al. (2010).

Water vapor has absorption features in the SWIR, but cannot account for any of the observed CTMF anomalies for CH_4. In this study, CH_4 and H_2O transmittance spectra with distinct absorptions across AVIRIS bands (Fig. 5) were used independently to generate CTMF results for CH_4 and H_2O. Although elevated water vapor levels could be co-located with CH_4 at all locations, CTMF results for water vapor indicate no contiguous H_2O anomalies at any location within the examined AVIRIS scenes.

CTMF results included a number of false positives that resulted from surfaces with strong absorptions similar to CH_4 absorption features, including oil-based paints and calcite. False positives generally appeared as contiguous pixels with a spatial shape that mimicked an underlying surface feature, for example individual rooftops. This suggests that the

AVIRIS spectral resolution limits the ability of the CTMF to accurately resolve between a pure CH_4 signature and land cover types with strong absorption features between 2200 and 2500 nm.

For AVIRIS scene r_04, a segmentation approach was used to reduce 'speckle' and isolate contiguous pixels with high CTMF scores, resulting in 16 segments. By applying a MESMA classification to reflectance spectra from these segments, segments were assigned to either a probable CH_4 anomalies or confusers class. As a result, anomalies located in close proximity to hydrocarbon storage tanks and in the office courtyard were assigned as true CH_4 anomalies. Despite being classified mostly as the confusers class, anomalies at the eastern edge of the La Brea Tar Pits were likely caused by absorption features resulting from the combination of CH_4 gas, oil, and tar present at this location.

While the CTMF approach is well suited for detecting anomalies, it does not provide concentrations necessary to calculate fluxes or generate maps of gas concentrations. However, a sensitivity analysis using synthetic images and Modtran 5.3 radiative transfer simulations currently is under development to determine the relationship between CTMF scores and CH_4 concentrations as well as the minimum detectable gas concentrations. This will permit a greater understanding of the limitations of the CTMF technique, including what types of emissions might go undetected. Residual based techniques using radiative transfer simulations are also being investigated as a means of quantifying gas concentrations (Dennison et al., 2011; Roberts et al., 2010). Evaluating the accuracy of these concentrations is an important prerequisite for creating maps of gas concentrations and estimating fluxes from individual point sources to better constrain regional emissions.

Given the high radiative forcing per CH_4 molecule and an abundance of point sources, targeting reductions in anthropogenic CH_4 is a particularly efficient means of mitigating its effects. High resolution mapping could permit emission monitoring from anthropogenic sources including wastewater treatment facilities, landfills, fossil fuel production, as well as sources of increasing concern like fugitive CH_4 emissions from leaking natural gas pipelines (Murdock et al., 2008) and hydraulic fracturing (Howarth et al., 2011). Recently, there has been concern over possible positive feedbacks between increased surface temperature and CH_4 released at high latitudes by melting permafrost (Woodwell et al., 1998), subsea permafrost (Shakhova et al., 2010), and from CH_4 hydrate destabilization (Kvenvolden, 1988). Therefore, developing remote sensing techniques to detect local emissions for terrestrial and marine environments could be particularly useful in monitoring potential increases in CH_4 emissions resulting from global warming.

5. Conclusions

High spatial resolution mapping of CH_4 over marine and terrestrial emission sources was performed using a CTMF technique applied to AVIRIS data. Prominent anomalies consistent with CH_4 emission from sonar-quantified seep bubble locations in the Coal Oil Point seep field were detected in addition to multiple anomalies located at known or probable emission sources in Los Angeles. The combined operations of segmentation of CTMF results followed by MESMA classification provides a means of semi-automatically discriminating between true CH_4 anomalies and false positives. Given that the CTMF results were quite consistent despite variations in input parameters, this technique is particularly well suited for application over large areas to detect CH_4 emissions from concentrated point sources.

With little modification, the CTMF algorithm could permit detection of additional greenhouse gasses with distinct absorption features, including CO_2 and N_2O (Dennison et al., 2013; Thorpe et al., 2012). The next generation AVIRIS sensor (AVIRISng) should be better suited for gas detection given it has a 5 nm spectral sampling and an improved signal-to-noise ratio (Hamlin et al., 2011). Further, proposed missions with AVIRIS-like sensors mounted on satellites including HyspIRI, EnMAP, Prisma, HYPXIM, and HISUI may be well-suited for detecting

emissions and could greatly improve mapping of regional emissions due to its high areal coverage and potential for repeat temporal coverage.

Acknowledgments

References

Aires, F., Chedin, A., Scott, N. A., & Rossow, W. B. (2002). A regularized neural net approach for retrieval of atmospheric and surface temperatures with the IASI instrument. *Journal of Applied Meteorology*, *41*, 144–159.

Beer, R., Glavich, T. A., & Rider, D. M. (2001). Tropospheric emission spectrometer for the Earth Observing System's Aura Satellite. *Applied Optics*, *40*, 2356–2367.

Bergamaschi, P., Krol, M., Meirink, J. F., Dentener, F., Segers, A., van Aardenne, J., Monni, S., Vermeulen, A. T., Schmidt, M., Ramonet, M., Yver, C., Meinhardt, F., Nisbet, E. G., Fisher, R. E., O'Doherty, S., & Dlugokencky, E. J. (2010). Inverse modeling of European CH_4 emissions 2001–2006. *Journal of Geophysical Research-Atmospheres*, *115*, D22309.

Berk, A., Bernstein, L. S., & Robertson, D. C. (1989). *MODTRAN: A moderate resolution model for LOWTRAN7, AFGL-TR-89-0122*. MA: Hanscom Air Force Base.

Bousquet, P., Ciais, P., Miller, J. B., Dlugokencky, E. J., Hauglustaine, D. A., Prigent, C., Van der Werf, G. R., Peylin, P., Brunke, E. G., Carouge, C., Langenfelds, R. L., Lathiere, J., Papa, F., Ramonet, M., Schmidt, M., Steele, L. P., Tyler, S. C., & White, J. (2006). Contribution of anthropogenic and natural sources to atmospheric methane variability. *Nature*, *443*, 439–443.

Bovensmann, H., Buchwitz, M., Burrows, J. P., Reuter, M., Krings, T., Gerilowski, K., Schneising, O., Heymann, J., Tretner, A., & Erzinger, J. (2010). A remote sensing technique for global monitoring of power plant CO_2 emissions from space and related applications. *Atmospheric Measurement Techniques*, *3*, 781–811.

Bradley, E. S., Leifer, I., Roberts, D. A., Dennison, P. E., & Washburn, L. (2011). Detection of marine methane emissions with AVIRIS band ratios. *Geophysical Research Letters*, *38*, L10702.

Buchwitz, M., de Beek, R., Burrows, J. P., Bovensmann, H., Warneke, T., Notholt, J., Meirink, J. F., Goede, A. P. H., Bergamaschi, P., Korner, S., Heimann, M., & Schulz, A. (2004). Atmospheric methane and carbon dioxide from SCIAMACHY satellite data: initial comparison with chemistry and transport models. *Atmospheric Chemistry and Physics*, *5*, 941–962.

Buchwitz, M., de Beek, R., Noel, S., Burrows, J. P., Bovensmann, H., Bremer, H., Bergamaschi, P., Korner, S., & Heimann, M. (2005). Carbon monoxide, methane and carbon dioxide columns retrieved from SCIAMACHY by WFM-DOAS: year 2003 initial data set. *Atmospheric Chemistry and Physics*, *5*, 3313–3329.

Buchwitz, M., Rozanov, V. V., & Burrows, J. P. (2000). A near-infrared optimized DOAS method for the fast global retrieval of atmospheric CH_4, CO, CO_2, H_2O, and N_2O total column amounts from SCIAMACHY Envisat-1 nadir radiances. *Journal of Geophysical Research-Atmospheres*, *105*, 15231–15245.

Butz, A., Guerlet, S., Hasekamp, O., Schepers, D., Galli, A., Aben, I., Frankenberg, C., Hartmann, J. M., Tran, H., Kuze, A., Keppel-Aleks, G., Toon, G., Wunch, D., Wennberg, P., Deutscher, N., Griffith, D., Macatangay, R., Messerschmidt, J., Notholt, J., & Warneke, T. (2011). Toward accurate CO_2 and CH_4 observations from GOSAT. *Geophysical Research Letters*, *38*, L14812.

Chilingar, G. V., & Endres, B. (2005). Environmental hazards posed by the Los Angeles Basin urban oilfields: an historical perspective of lessons learned. *Environmental Geology*, *47*, 302–317.

Clark, R., Swayze, G., Livo, E., Kokaly, R., King, T. V. V., Dalton, B., Vance, S., Rockwell, B., Hoefen, T., & McDougal, R. (2002). *Surface reflectance calibration of terrestrial imaging spectroscopy data: a tutorial using AVIRIS: proceedings of the 11th JPL Airborne Earth Science Workshop*. Pasadena, California: Jet Propulsion Laboratory Publications.

Clark, J. F., Washburn, L., & Emery, K. S. (2010). Variability of gas composition and flux intensity in natural marine hydrocarbon seeps. *Geo-Marine Letters*, *30*, 379–388.

Cliff, A. D., & Ord, J. K. (1981). *Spatial processes, models and applications*. London: Pion (266 pp.).

Dennison, P. E., Qi, Y., Thorpe, A. K., Pardyjak, E. R., Roberts, D. A., & Funk, C. C. (2011). High spatial resolution mapping of power plant CO_2 plumes using imaging spectrometer data. *American Geophysical Union Fall Meeting. San Francisco, CA*.

Dennison, P. E., & Roberts, D. A. (2003). Endmember selection for multiple endmember spectral mixture analysis using endmember average RMSE. *Remote Sensing of Environment*, *87*, 123–135.

Dennison, P. E., Thorpe, A. K., Qi, Y., Roberts, D. A., Green, R. O., Bradley, E. S., Funk, C. C. (2013). High spatial resolution mapping of elevated atmospheric carbon dioxide using airborne imaging spectroscopy: Radiative transfer modeling and power plant plume detection. *Remote Sensing of Environment*, in revision.

Dlugokencky, E. J., Bruhwiler, L., White, J. W. C., Emmons, L. K., Novelli, P. C., Montzka, S. A., Masarie, K. A., Lang, P. M., Crotwell, A. M., Miller, J. B., & Gatti, L. V. (2009). Observational constraints on recent increases in the atmospheric CH_4 burden. *Geophysical Research Letters*, *36*, L18803.

Dlugokencky, E. J., Nisbet, E. G., Fisher, R., & Lowry, D. (2011). Global atmospheric methane: Budget, changes and dangers. *Philosophical Transactions of the Royal Society A - Mathematical Physical and Engineering Sciences*, *369*, 2058–2072.

DOGGR (2010a). *GIS and well data downloads*. State of California Department of Conservation, Division of Oil, Gas & Geothermal Resources (DOGGR) (http://www.consrv.ca. gov/dog/maps/Pages/goto_welllocation.aspx)

DOGGR (2010b). *Online production and injection query*. State of California Department of Conservation, Division of Oil, Gas & Geothermal Resources (DOGGR) (http://opi.consrv. ca.gov/opi/opi.dll)

EPA (2010). *Producers technology transfer workshop: Reducing methane emission with vapor recovery on storage tanks, lessons learned from the natural gas STAR program*. Vernal, Utah: United States Environmental Protection Agency (EPA).

EPA (2011). *Inventory of U.S. greenhouse gas emissions and sinks: 1990–2009*. Washington, D.C. United States Environmental Protection Agency (EPA).

Etiope, G., Feyzullayev, A., & Baciu, C. L. (2009). Terrestrial methane seeps and mud volcanoes: A global perspective of gas origin. *Marine and Petroleum Geology*, *26*, 333–344.

Farrell, P., Culling, D., & Leifer, I. (2013). Transcontinental Methane Measurements: Part 1. A Mobile Surface Platform for Source Investigations. *Atmospheric Environment* (in press).

Frankenberg, C., Aben, I., Bergamaschi, P., Dlugokencky, E. J., van Hees, R., Houweling, S., van der Meer, P., Snel, R., & Tol, P. (2011). Global column-averaged methane mixing ratios from 2003 to 2009 as derived from SCIAMACHY: Trends and variability. *Journal of Geophysical Research-Atmospheres*, *116*, D04302.

Frankenberg, C., Meirink, J. F., van Weele, M., Platt, U., & Wagner, T. (2005). Assessing methane emissions from global space-borne observations. *Science*, *308*, 1010–1014.

Funk, C. C., Theiler, J., Roberts, D. A., & Borel, C. C. (2001). Clustering to improve matched filter detection of weak gas plumes in hyperspectral thermal imagery. *IEEE Transactions on Geoscience and Remote Sensing*, *39*, 1410–1420.

Green, R. O., Eastwood, M. L., Sarture, C. M., Chrien, T. G., Aronsson, M., Chippendale, B. J., Faust, J. A., Pavri, B. E., Chovit, C. J., Solis, M. S., Olah, M. R., & Williams, O. (1998). Imaging spectroscopy and the Airborne Visible Infrared Imaging Spectrometer (AVIRIS). *Remote Sensing of Environment*, *65*, 227–248.

Gurevich, A. E., Endres, B. L., Robertson, J. O., & Chilingar, G. V. (1993). Gas migration from oil and gas fields and associated hazards. *Journal of Petroleum Science and Engineering*, *9*, 223–238.

Hamlin, L., Green, R. O., Mouroulis, P., Eastwood, M., Wilson, D., Dudik, M., & Paine, C. (2011). Imaging spectrometer science measurements for terrestrial ecology: AVIRIS and new developments. *Aerospace Conference, 2011 IEEE*.

Herold, M., Roberts, D. A., Gardner, M. E., & Dennison, P. E. (2004). Spectrometry for urban area remote sensing — Development and analysis of a spectral library from 350 to 2400 nm. *Remote Sensing of Environment*, *91*, 304–319.

Hornafius, J. S., Quigley, D., & Luyendyk, B. P. (1999). The world's most spectacular marine hydrocarbon seeps (Coal Oil Point, Santa Barbara Channel): Quantification of emissions. *Journal of Geophysical Research - Oceans*, *104*, 20703–20711.

Howarth, R. W., Santoro, R., & Ingraffea, A. (2011). Methane and the greenhouse-gas footprint of natural gas from shale formations. *Climatic Change*, *106*, 679–690.

Hsu, Y. K., VanCuren, T., Park, S., Jakober, C., Herner, J., FitzGibbon, M., Blake, D. R., & Parrish, D. D. (2010). Methane emissions inventory verification in southern California. *Atmospheric Environment*, *44*, 1–7.

IPCC (2000). *Good Practice Guidance and Uncertainty Management in National Greenhouse Gas Inventories, Report of the Intergovernmental Panel on Climate Change*. New York: Cambridge Univ. Press.

IPCC (2007). *Climate Change 2007: The Physical Science Basis. Contribution of Working Group I to the Fourth Assessment Report of the Intergovernmental Panel on Climate Change*. New York: Cambridge Univ. Press.

Kvenvolden, K. A. (1988). Methane hydrate — A major reservoir of carbon in the shallow geosphere. *Chemical Geology*, *71*, 41–51.

Kvenvolden, K. A., & Rogers, B. W. (2005). Gaia's breath — Global methane exhalations. *Marine and Petroleum Geology*, *22*, 579–590.

Leifer, I., Kamerling, M. J., Luyendyk, B. P., & Wilson, D. S. (2010). Geologic control of natural marine hydrocarbon seep emissions, Coal Oil Point seep field, California. *Geo-Marine Letters*, *30*, 331–338.

Leifer, I., Luyendyk, B. P., Boles, J., & Clark, J. F. (2006a). Natural marine seepage blowout: Contribution to atmospheric methane. *Global Biogeochemical Cycles*, *20*, GB3008.

Leifer, I., Roberts, D., Margolis, J., & Kinnaman, F. (2006b). In situ sensing of methane emissions from natural marine hydrocarbon seeps: A potential remote sensing technology. *Earth and Planetary Science Letters*, *245*, 509–522.

Lelieveld, J., Crutzen, P. J., & Bruhl, C. (1993). Climate effects of atmospheric methane. *Chemosphere*, *26*, 739–768.

Lelieveld, J., Crutzen, P. J., & Dentener, F. J. (1998). Changing concentration, lifetime and climate forcing of atmospheric methane. *Tellus Series B: Chemical and Physical Meteorology*, *50*, 128–150.

Montzka, S. A., Dlugokencky, E. J., & Butler, J. H. (2011). Non-CO_2 greenhouse gases and climate change. *Nature*, *476*, 43–50.

Murdock, D. G., Stearns, S. V., Lines, R. T., Lenz, D., Brown, D. M., & Philbrick, C. R. (2008). Applications of real-world gas detection: Airborne Natural Gas Emission Lidar (ANGEL) system. *Journal of Applied Remote Sensing*, *2*, 023518.

NOAA (2012). *GMD measurement locations*. : National Oceanic & Atmospheric Administration (NOAA), Earth System Research Laboratory, Global Monitoring Division (http://www.esrl.noaa.gov/gmd/dv/iadv/index.php)

NRC (2010). *Verifying Greenhouse Gas Emissions: Methods to Support International Climate Agreements. Committee on Methods for Estimating Greenhouse Gas Emissions; National Research Council*. Washington, D.C.: The National Academies Press.

Parker, R., Boesch, H., Cogan, A., Fraser, A., Feng, L., Palmer, P. I., Messerschmidt, J., Deutscher, N., Griffith, D. W. T., Notholt, J., Wennberg, P. O., & Wunch, D. (2011).

Methane observations from the Greenhouse Gases Observing SATellite: Comparison to ground-based TCCON data and model calculations. *Geophysical Research Letters, 38*.

Pipkin, B. W., & Proctor, R. J. (Eds.). (1992). *Engineering Geology Practice in Southern California, Special Publication No. 4, Association of Engineering Geologists, Southern California Section.*. Belmont, California: Star Publishing Company.

Roberts, D. A., Bradley, E. S., Cheung, R., Leifer, I., Dennison, P. E., & Margolis, J. S. (2010). Mapping methane emissions from a marine geological seep source using imaging spectrometry. *Remote Sensing of Environment, 114*, 592–606.

Roberts, D. A., Gardner, M., Church, R., Ustin, S., Scheer, G., & Green, R. O. (1998). Mapping chaparral in the Santa Monica Mountains using multiple endmember spectral mixture models. *Remote Sensing of Environment, 65*, 267–279.

Roberts, D. A., Green, R. O., & Adams, J. B. (1997). Temporal and spatial patterns in vegetation and atmospheric properties from AVIRIS. *Remote Sensing of Environment, 62*, 223–240.

Roberts, D. A., Quattrochi, D. A., Hulley, G. C., Hook, S. J., & Green, R. O. (2012). Synergies between VSWIR and TIR data for the urban environment: An evaluation of the potential for the Hyperspectral Infrared Imager (HyspIRI) Decadal Survey mission. *Remote Sensing of Environment, 117*, 83–101.

Saitoh, N., Imasu, R., Ota, Y., & Niwa, Y. (2009). CO_2 retrieval algorithm for the thermal infrared spectra of the Greenhouse Gases Observing Satellite: Potential of retrieving CO_2 vertical profile from high-resolution FTS sensor. *Journal of Geophysical Research-Atmospheres, 114*.

Schepers, D., Guerlet, S., Butz, A., Landgraf, J., Frankenberg, C., Hasekamp, O., Blavier, J. F., Deutscher, N. M., Griffith, D. W. T., Hase, F., Kyro, E., Morino, I., Sherlock, V., Sussmann, R., & Aben, I. (2012). Methane retrievals from Greenhouse Gases Observing

Satellite (GOSAT) shortwave infrared measurements: Performance comparison of proxy and physics retrieval algorithms. *Journal of Geophysical Research-Atmospheres, 117*.

Shakhova, N., Semiletov, I., Salyuk, A., Yusupov, V., Kosmach, D., & Gustafsson, O. (2010). Extensive methane venting to the atmosphere from sediments of the East Siberian Arctic Shelf. *Science, 327*, 1246–1250.

Theiler, J., & Foy, B. R. (2006). Effect of signal contamination in matched-filter detection of the signal on a cluttered background. *IEEE Geoscience and Remote Sensing Letters, 3*, 98–102.

Thorpe, A. K., Roberts, D. A., Dennison, P. E., Bradley, E. S., & Funk, C. C. (2012). Point source emissions mapping using the Airborne Visible/Infrared Imaging Spectrometer (AVIRIS). *Proceedings of SPIE, 8390*, 839013.

Tobin, D. C., Revercomb, H. E., Moeller, C. C., & Pagano, T. S. (2006). Use of atmospheric infrared sounder high-spectral resolution spectra to assess the calibration of Moderate resolution Imaging Spectroradiometer on EOS Aqua. *Journal of Geophysical Research-Atmospheres, 111*, D09S05.

Townsend-Small, A., Tyler, S. C., Pataki, D. E., Xu, X. M., & Christensen, L. E. (2012). Isotopic measurements of atmospheric methane in Los Angeles, California, USA: Influence of "fugitive" fossil fuel emissions. *Journal of Geophysical Research-Atmospheres, 117*.

Villeneuve, P. V., Fry, H. A., Theiler, J. P., Clodius, W. B., Smith, B. W., & Stocker, A. D. (1999). Improved matched-filter detection techniques. *Proceedings of SPIE, 3753*, 278–285.

Woodwell, G. M., Mackenzie, F. T., Houghton, R. A., Apps, M., Gorham, E., & Davidson, E. (1998). Biotic feedbacks in the warming of the earth. *Climatic Change, 40*, 495–518.

Wunch, D., Wennberg, P. O., Toon, G. C., Keppel-Aleks, G., & Yavin, Y. G. (2009). Emissions of greenhouse gases from a North American megacity. *Geophysical Research Letters, 36*, L15810.